PCCP

PAPER

View Article Online
View Journal | View Issue

Cite this: *Phys. Chem. Chem. Phys.*, 2019, **21**, 10185

Blind spheres of paramagnetic dopants in solid state NMR†

Wenyu Li, [a] Qianyun Zhang, [a] Jonas J. Joos, [b] Philippe F. Smet [b] and Jörn Schmedt auf der Günne *[a]

Received 17th February 2019,
Accepted 29th April 2019

DOI: 10.1039/c9cp00953a

rsc.li/pccp

Solid-state NMR on paramagnetically doped crystal structures gives information about the spatial distribution of dopants in the host. Paramagnetic dopants may render NMR active nuclei virtually invisible by relaxation, paramagnetic broadening or shielding. In this contribution blind sphere radii r_0 have been reported, which could be extracted through fitting the NMR signal visibility function $f(x) = \exp(-ar_0^3x)$ to experimental data obtained on several model compound series: $La_{1-x}Ln_xPO_4$ (Ln = Nd, Sm, Gd, Dy, Ho, Er, Tm, Yb), $Sr_{1-x}Eu_xGa_2S_4$ and $(Zn_{1-x}Mn_x)_3(PO_4)_2{\cdot}4H_2O$. Radii were extracted for ^{1}H, ^{31}P and ^{71}Ga, and dopants like Nd^{3+}, Gd^{3+}, Dy^{3+}, Ho^{3+}, Er^{3+}, Tm^{3+}, Yb^{3+} and Mn^{2+}. The observed radii determined differed in all cases and covered a range from 5.5 to 13.5 Å. While these radii were obtained from the amount of invisible NMR signal, we also show how to link the visibility function to lineshape parameters. We show under which conditions empirical correlations of linewidth and doping concentration can be used to extract blind sphere radii from second moment or linewidth parameter data. From the second moment analysis of $La_{1-x}Sm_xPO_4$ ^{31}P MAS NMR spectra for example, a blind sphere size of Sm^{3+} can be determined, even though the visibility function remains close to 100% over the entire doping range. Dependence of the blind sphere radius r_0 on the NMR isotope and on the paramagnetic dopant could be suggested and verified: for different nuclei, r_0 shows a $\sqrt[3]{\gamma}$-dependence, γ being the gyromagnetic ratio. The blind sphere radii r_0 for different paramagnetic dopants in a lanthanide series could be predicted from the pseudo-contact term.

Introduction

Nuclear magnetic resonance (NMR) has contributed to the study of paramagnetic systems, such as in structural biology,[1–5] battery materials,[6–8] characterization of pharmaceutical formulation,[9,10] polymers,[11,12] chemical shift thermometers[13,14] and luminescent materials.[15–23] The range of applications of paramagnetic NMR is surprising given that the strong electronic magnetic moment of the paramagnetic species interferes with the NMR measurement in different ways. Nevertheless, paramagnetic NMR may give information about structure,[2,12] dynamics[8,24] and the distribution of paramagnetic dopants in a host.[17–22,25,26] In the latter case different approaches had been used namely relaxation times,[19,20,22] linewidths[17,18] and observed peaks areas[21,25] to relate doping homogeneity to the performance of these luminescent materials.

In solid-state NMR a distinction needs to be made between lanthanide atoms and transition metal atoms. The influence transition metal atoms exert on neighbouring NMR nuclei enables studies for example on battery materials[6–8] or metal organic framework compounds.[27] The computation of the influence on valence electrons is important and progress in the computation of paramagnetic shifts[28] has improved significantly in recent years. In contrast, lanthanides with few exceptions show hardly any influence from the valence shell and thus have been used for systematic experimental studies to identify contributions to the paramagnetic spin Hamiltonian.[28,29] Paramagnetic NMR of lanthanide containing compounds found various applications to luminescent materials.[15–21]

A non-trivial problem to paramagnetic NMR is that NMR resonances of paramagnetic compounds may virtually vanish in the dead-time of the NMR spectrometer by relaxation, inhomogeneous broadening mechanisms or anisotropic susceptibility broadening.[29] Lineshape analysis as proposed by Van Vleck[30] in terms of moment-analysis or NMR line width comes with a visibility caveat. Nevertheless, this approach was proved successful in the characterization of several phosphors,[17,18] where it could be shown that, as expected by van Vleck, the linewidth depended linearly on the paramagnetic doping level x at low doping concentration. It should be noted that in the high

[a] *Inorganic Materials Chemistry, University of Siegen, Adolf-Reichwein-Str. 2, 57076 Siegen, Germany. E-mail: gunnej@chemie.uni-siegen.de*
[b] *LumiLab, Department of Solid State Sciences, Ghent University, Krijgslaan 281-S1, 9000 Gent, Belgium*

† Electronic supplementary information (ESI) available: Numerical for the spectral analysis of $LaPO_4$:Sm, EXSY spectra for $LaPO_4$:Ln, ^{31}P NMR relaxation data for $LaPO_4$:Ln. See DOI: 10.1039/c9cp00953a

doping regime a non-trivial dependence due to "exchange narrowing"[30–32] may lead to deviations from this simple behaviour. In case of luminescent materials, the doping homogeneity is of major importance to establish an optimal performance.[33,34] When luminescent ions are too close, energy can easily be transferred between them, leading to uncontrollable migration of energy in the dopant sublattice that can eventually be non-radiatively dissipated at so-called luminescence killer centres. This effect is usually referred to as concentration quenching[35,36] and has been related to the dopant distribution obtained from NMR lineshape analysis in a few cases.[17,18] Furthermore, it was evidenced by a microscopic investigation that the thermal quenching behaviour, *i.e.* the decrease of luminescence quantum yield for increasing temperatures,[37] is severely worsened for inhomogeneously doped materials due to areas with a locally more elevated doping concentration.[34]

Instead of asking for the NMR properties of the visible paramagnetic signals, it may be interesting to ask for the fraction of NMR invisible signal. If a spherical regime around a paramagnetic centre is assumed, from which no NMR signals can be detected, it is possible to relate the signal loss to the size of this sphere of influence which is known under the name blind-sphere[38,39] or wipe-out radius.[40–42] Such radii are important in solution NMR[38,39] where paramagnetic constraints are used for structure solution, and in dynamic nuclear polarization (DNP) to estimate the zone which cannot be accessed by NMR[43–45] and for luminescent materials to study doping homogeneity.[21]

Spectroscopically the blind sphere can be explained by line broadening which leads to undetectable signal by standard experiments,[39] or signal shift[46] that puts the signal outside of spectral window. The origins of blind sphere may relate to (but are not limited to) the following contributions:[39] relaxation which may involve dipolar, Curie, contact and cross relaxation mechanisms, and hyperfine shift which contains contact and pseudo-contact parts.

Reported sizes of blind spheres have been mostly related to the solution NMR, for which Bertini[39] and co-workers have laid a foundation. Besides some attempts have been made to quantify the blind sphere radius of DNP polarizing agents.[43,47] In solid state, due to anisotropic interactions and more ambiguous estimation of correlation time τ_c and spectral density function $J(\omega)$, blind sphere sizes may differ and questions about the influence that a paramagnetic centre has on its environment remain open. To the best of our knowledge, for solid crystalline samples a systematic study on the sizes of blind spheres of different inorganic dopants has not been published before.

The target of this contribution is to relate the size of blind spheres of solid samples to other physical quantities, for example the gyromagnetic ratio of NMR nuclei and the effective magnetic moment of the paramagnetic ion by studying the blind sphere radii in lanthanide-doped solid solutions. Moreover, given that doping homogeneity of inorganic phosphors can be traced both *via* the visible signal by lineshape analysis and *via* the fraction of the invisible signal,[21] it is natural to ask whether the blind sphere radius and linewidth or moment analysis can be linked, and if so under which conditions.

Experimental

The $La_{1-x}Ln_xPO_4$ (Ln = Nd, Sm, Gd, Dy, Er, Ho, Tm, Yb) samples have been synthesized *via* a co-precipitation method: Ln_2O_3 (Nd_2O_3 was bought from chemPUR, the rest from smart elements, the purity is 99.999% for Dy_2O_3 and 99.99% for the rest) and La_2O_3 (chemPUR, 99.99%) were dissolved in nitric acid and later on mixed with $NH_4H_2PO_4$ (VWR chemicals) solution. The resulting precipitates were dried at 80 °C overnight, sintered in corundum crucibles at 1000 °C for 4 h.

$Sr_{1-x}Eu_xGa_2S_4$ powders were obtained *via* a solid state synthesis method. Stoichiometric quantities of SrS (Alfa Aesar, 99.9%), Ga_2S_3 (Alfa Aesar, 99.99%) and EuF_3 (Alfa Aesar, 99.5%) were weighed and mixed in an agate mortar. A small amount (1 weight %) of NH_4F (Alfa Aesar, 98+%) was added as a fluxing agent. The mixtures were fired for two hours at 900 °C under a flow of forming gas (90% N_2, 10% H_2). The obtained powder was again lightly ground.

The $(Zn_{1-x}Mn_x)_3(PO_4)_2{\cdot}4H_2O$ samples have been synthesized by a co-precipitation method: stoichiometric amounts of $MnCl_2{\cdot}4H_2O$ (ACROS organics, 99+%) and $Zn(NO_3)_2{\cdot}6H_2O$ (chemPUR, 98+%) were dissolved into water and mixed with an excess of $NH_4H_2PO_4$ (VWR chemicals) in aqueous solution. The precipitates were washed with water and ethanol and dried overnight.

Powder X-ray diffraction (XRD) measurements were performed on a Huber G621 diffractometer with Cu $K_{\alpha 1}$ radiation (λ = 0.15405931 nm) in transmission geometry. Diffractograms were extracted from the image files, which were obtained by scanning the photostimulable $BaBrF:Eu^{2+}$ films with an image plate detector (Typhoon FLA 7000, λ = 650 nm), by home-written program ipreader-0.9. The Rietveld analysis was performed *via* the program TOPAS-Academic (TOtal PAttern Solution, by Coelho Software, V4.1).

The solid state NMR measurements were performed on a Bruker Avance II spectrometer at a magnetic field of 7.05 T. Magic angle spinning (MAS) was done with 4 mm pencil rotors at spinning frequencies of 10 kHz or 12.5 kHz with a home-built McKay probe head. The dead time delay was set to 15 μs. Quantification was assisted by a micro-balance (Sartorius MC5). The deconvolution of peaks and moment analysis were assisted with the program deconv2Dxy[48] (version 0.4). The NMR visibility fitting function[21] for a homogeneously doped sample is defined as follows.

$$f(x) = \exp(-ar_0^3 x) \quad (1)$$

The wipe-out radius r_0 relates to the size of the blind sphere of a paramagnetic centre and the variable a is host-specific number ($a = 4\pi N_{\mathrm{hostUC}}/3V_{\mathrm{UC}}$ where N_{hostUC} is the number of "dopable" sites in the unit cell and V_{UC} is the volume of the unit cell). For monazite[49] $LaPO_4$ the variable a amounts to 0.055 $Å^{-3}$. The doping concentration x in this work is defined as the degree of substitution, which is dimensionless. The experimental NMR visibility f was calculated in the following way: first the molar peak areas $P = A/n$ were calculated for all samples in one dopant series (A peak area, n amount of material).

The visibility function $f(x)$ and $P(x)$ are related by normalization through the undoped sample, *i.e.* $P(x) = f(x)\cdot P(0)$. Therefore the experimental P values were fitted with the function $P(x)$ to determine the free parameters r_0 and $P(0)$. This approach gives equal weight to all measured points. The diagrams (Fig. 2, 4, 7 and 8) show $P(x)/P(0)$ on the y-axis.

Results and discussion

The target of this contribution is to provide a better understanding of the blind sphere in solids. In order to achieve that, measurements have been performed on three model compounds series, Ln^{3+} (Ln = Nd, Sm, Gd, Dy, Er, Ho, Tm, Yb) doped monazite $LaPO_4$, Mn^{2+} doped hopeite $Zn_3(PO_4)_2{\cdot}4H_2O$ and Eu^{2+} doped $SrGa_2S_4$. Lanthanide doped xenotime YPO_4 and monazite $LaPO_4$ have been subject to several studies50,51 in terms of a determination of NMR parameters. Lanthanide dopants have the advantage that for a model study chemical interference is reduced to a minimum because of the low lying, unpaired *f*-shell electrons. To extract the sizes of blind spheres from measured data, approaches which relate the peak area and lineshape to the doping level are investigated. Finally, the obtained sizes are compared to establish relations between blind sphere and physical quantities, for example magnetic moment and gyromagnetic ratio.

Peak area and blind sphere

To judge the quality of obtained samples X-ray diffraction was applied. The synthesized samples were phase pure according to X-ray diffraction. Rietveld refinements of the diffraction pattern yielded lattice parameters which followed Vegard's law.[52] Fig. 1 shows the lattice parameters of $La_{1-x}Sm_xPO_4$ follow a linear dependence on the doping concentration x as an example. Such a fulfilment of Vegard's law is often considered as evidence for a homogeneously doped phase pure sample in the sense of a solid solution.

The single pulse ^{31}P MAS NMR spectra offer information on the change of peak area upon increasing the doping level x. Based on the visibility function[21] $f(x) = \exp(-ar_0{}^3x)$ blind sphere radii for trivalent dopants Ln^{3+} (Ln = Nd, Gd, Dy, Er, Ho, Tm, Yb) could be obtained (Fig. 2 and Table 1).

While in principle blind sphere radii can be determined from two points only, we fitted the visibility function to all points (experimental part). Because of the discrete nature of the pair distribution function in crystalline materials, radii determined this way become less reliable the smaller the blind-sphere radius (see discussion in ref. 21).

Line shape and blind sphere

While the visibility function $f(x) = \exp(-ar_0{}^3x)$ proved to be a useful tool for the extraction of blind-sphere radii in the cases above and in case of $Sr_{1-x}Eu_xH_2$,[21] it could not be applied in case of $La_{1-x}Sm_xPO_4$, because single pulse ^{31}P MAS NMR (Fig. 3) recovers (Fig. 4) signals from all ^{31}P atoms including those of the first coordination sphere around Sm^{3+}, as can be seen from the visibility function (Fig. 4 in circles) which stays close to 100% for all doping concentrations x.

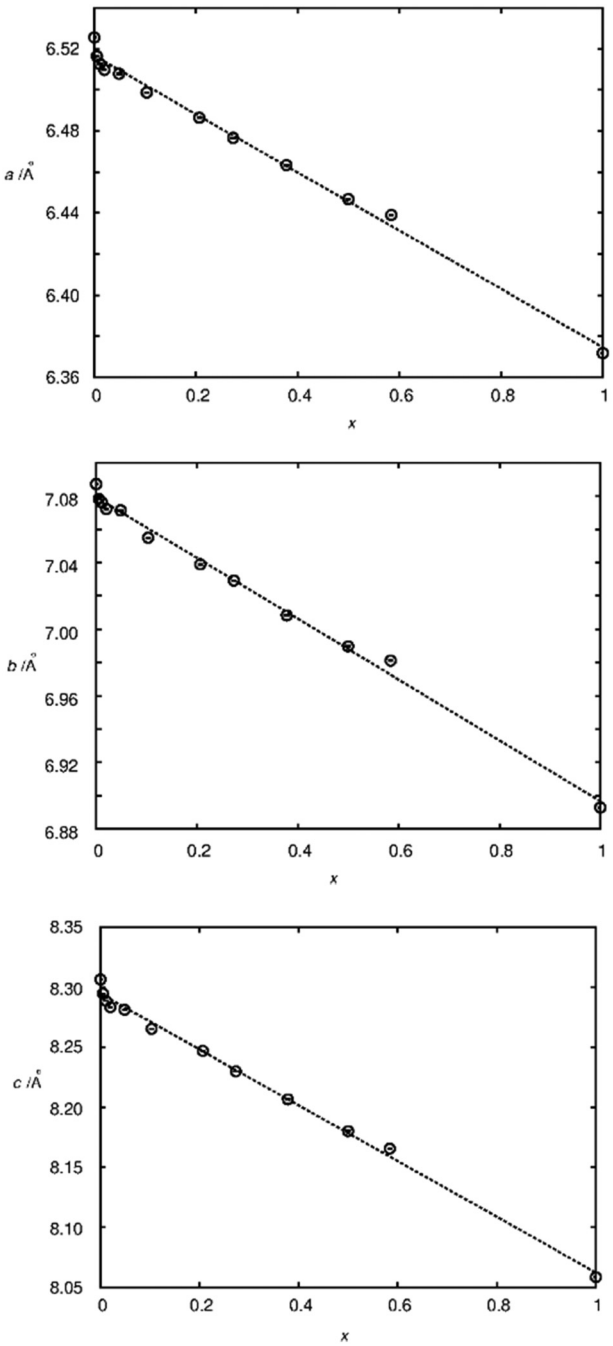

Fig. 1 Lattice parameters as a function of the substitution degree x in $La_{1-x}Sm_xPO_4$, as determined by Rietveld refinement based on X-ray powder diffraction data. The dotted lines represent linear fits resulting in a/Å = 6.516 − 0.142·x, b/Å = 7.0794 − 0.183·x, c/Å = 8.294 − 0.232·x.

Because of line broadening, precise deconvolution of different environments is difficult for $x > 0.1$. Despite the large errors from peak deconvolution, an analysis was attempted to relate line width and doping concentration (ESI,† Fig. S1) as previously done on similar systems in literature,[17,18] however, a linear dependence could not be found. On the other hand a signal specific

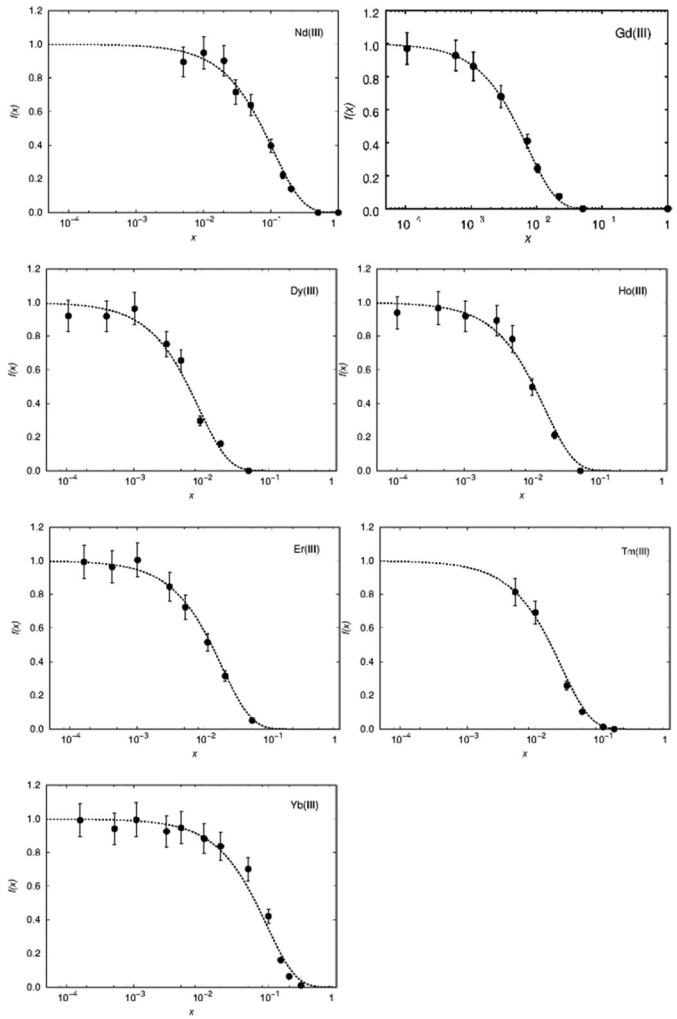

Fig. 2 Normalized visibility function f (circles with error bars) calculated from ^{31}P MAS NMR data plotted against the substitution degree x in $La_{1-x}Ln_xPO_4$, on a logarithmic scale. The dashed line corresponds to the fitting function $f(x) = \exp(-ar_0^3x)$ with a = 0.055 Å^{-3} and r_0 = 5.5, 13.5, 12.5, 10.5, 10, 9 and 5.8 Å for Ln = Nd, Gd, Dy, Ho, Er, Tm and Yb, respectively.

Table 1 Radii of blind spheres r_0 obtained from ^{31}P MAS NMR of $La_{1-x}Ln_xPO_4$ sample series, the effective magnetic moments[53] μ_{eff} in equivalents of the Bohr magneton μ_B and the number of unpaired 4f electrons $N_{unpaired}$ for comparison; r_0 determined by peak area method except for "*" where an estimate from second moment analysis is reported (see main text)

Dopant ion	r_0/Å	μ_{eff}/μ_B	$N_{unpaired}$
Nd^{3+}	5.5	3.62	3
Sm^{3+}	0.45*	1.54	5
Gd^{3+}	13.5	7.95	7
Dy^{3+}	12.5	10.5	5
Ho^{3+}	10.5	10.5	4
Er^{3+}	10.0	9.55	3
Tm^{3+}	9.0	7.5	2
Yb^{3+}	5.8	4.4	1

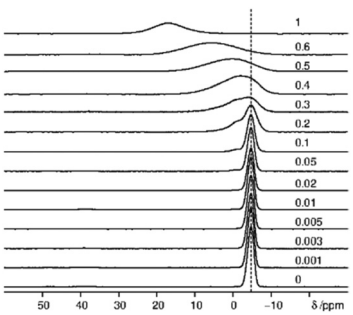

Fig. 3 Stack plot of ^{31}P MAS NMR spectra of $La_{1-x}Sm_xPO_4$ (x values are marked on the corresponding spectra, dashed line indicates the position of the peak of pure $LaPO_4$).

^{31}P visibility function f can be defined, which corresponds only to the area of the peak which has a similar shift and linewidth as the peak of pure host material $LaPO_4$ (Fig. 4, triangles). A radius of 4.5 Å could in principle be obtained this way which as expected covers the P-atoms in the first coordination sphere around the La atom.

A practical approach which works for any kind of lineshape is to calculate the second moment from the lineshape as suggested by Van Vleck[30] in the context of dipolar peak broadening on whole spectra, which does not rely on the separation of different environments. This dipolar broadening includes

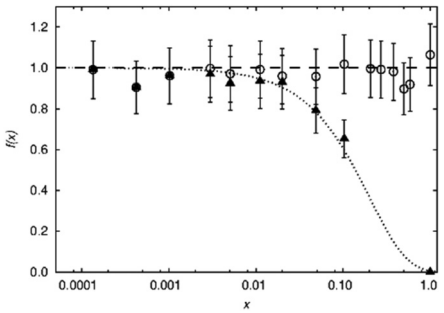

Fig. 4 Normalized visibility $f(x)$ of the ^{31}P MAS NMR signal of $La_{1-x}Sm_xPO_4$. The circles represent the $f(x)$ values calculated from whole peak area, which scatter around 100% (dashed line). The triangles represent the $f(x)$ values from the sharp component which has a similar isotropic chemical shift value as the pure $LaPO_4$. The dotted line refers to the fitting function $f(x) = \exp(-ar_0^3x)$ with a = 0.055 Å^{-3} and r_0 = 4.5 Å. Note that this r_0 does not follow the definition used in the rest of this contribution.

broadening by magnetic dipolar couplings because of the hyperfine coupling. In case of $La_{1-x}Sm_xPO_4$ the second moment M_2/Hz^2 follows the doping concentration x in a linear way over a wide range (Fig. 5).

To explain the observed linear relation, a brief discussion of line shape functions and line broadening mechanisms may be helpful. For an idealized free induction decay (FID) of a single nucleus the decay function can be expressed for example as a Gaussian or monoexponentially decaying function. The Fourier transformation of such a FID returns a Gaussian or Lorentzian line shape, respectively. When a resonance is broadened homogeneously, for example by relaxation *i.e.* by random oscillatory local field components at the Larmor frequency[54] or by lifetime broadening,[29] then the Lorentzian function is a good basis for the description of the line-shape in the frequency domain. On the other hand, inhomogeneous broadening,[55,56] which can be caused for example by magnetic field inhomogeneity, chemical shift anisotropy (CSA) or pseudo-contact term, produces a more complicated, often asymmetric lineshape, for which the description by van Vleck's moment approach is a suitable analysis tool. In van Vleck's moment approach, the dipolarly broadened spectral lineshape is decomposed into a sum of Gaussian functions. Hole-burning[57–59] experiments allow to distinguish inhomogeneous from homogeneous broadening.

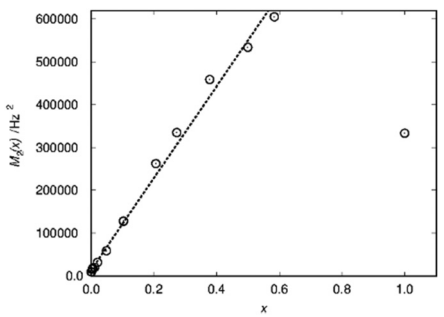

Fig. 5 Second moment $M_2(x)$ as a function of the substitution degree x in $La_{1-x}Sm_xPO_4$. The dotted line represents linear fit resulting in M_2/Hz^2 = $1.4 \times 10^4 + 1.07 \times 10^6 \cdot x$.

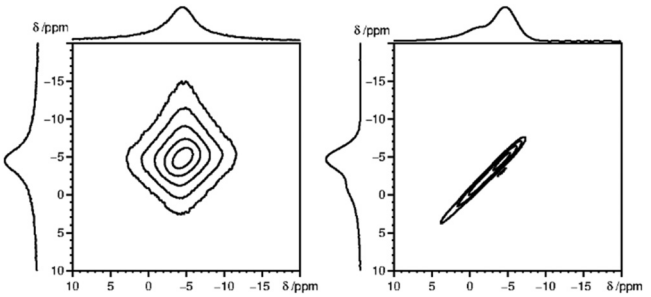

Fig. 6 2D ^{31}P MAS EXSY spectra (with zero mixing time) for $La_{0.997}Gd_{0.003}PO_4$ (left) and $La_{0.99}Sm_{0.01}PO_4$ (right), which depicted homogeneous and inhomogeneous type of line broadening, respectively.

A simple alternative to the hole-burning experiment is the 2D exchange spectroscopy (EXSY) experiment. EXSY experiments with zero mixing time show a sharp ridge on the diagonal in case of inhomogeneous broadening and a double Lorentzian type lineshape in case of homogeneous broadening. Note that the EXSY looks the same and behaves like the stimulated echo experiment. From the ^{31}P MAS NMR 2D spectra (Fig. 6), it is clear that the ^{31}P 2D NMR signal observed for Sm^{3+} doped $LaPO_4$ is typical for inhomogeneous broadening, while for Gd^{3+} homogeneous broadening is observed. The ^{31}P NMR signals for the other measured Ln^{3+} doped samples, namely Nd^{3+}, Dy^{3+}, Ho^{3+}, Er^{3+}, Tm^{3+} and Yb^{3+}, all show an inhomogeneous broadening behaviour (ESI,† Fig. S2).

In the following, a relation between the blind-sphere radius and the observed line-broadening is developed for simple cases.

The peak area which is the basis of the visibility function $f(x)$ (see above) is related to the intensity of first point of the FID according to the integral theorem of the Fourier transformation.[56] Any loss in peak area should then be reflected by the decay of the FID during the dead-time delay t_{de}, either by relaxation or by coherent mechanisms. If spectral line-broadening is assumed to be following a simple Lorentzian or Gaussian function then the decay in the FID needs to be monoexponential or Gaussian, respectively. Thus for simple cases the blind-sphere radius and line-broadening follow simple analytical expressions for a given dead-time delay (see below).

A Gaussian type FID $s_G(t)$ of an on-resonance signal is described with a linewidth parameter λ_G and the amplitude factor $s_{G,0}$.

$$s_G(t) = s_{G,0}\exp(-{\lambda_G}^2t^2) \quad (2)$$

The corresponding spectral function $I_G(\omega)$ is obtained by a single-sided complex Fourier transformation.[56]

$$\begin{aligned} I_G(\omega) &= \frac{1}{\pi}\int_0^\infty s_G(t)e^{-i\omega t}dt \\ &= \frac{s_{G,0}}{\sqrt{\pi}2\lambda_G}\exp\left(-\frac{\omega^2}{4{\lambda_G}^2}\right)\left[1 - i\mathrm{erfi}\left(\frac{\omega}{2\lambda_G}\right)\right] \end{aligned} \quad (3)$$

The line width parameter λ_G is related to the full width half-maximum of the line-shape in Hz as $\lambda_G = \frac{\pi}{2\sqrt{\ln 2}}\Delta\nu_G^{FWHM}$.

Given the lineshape of a paramagnetically doped sample can be described with a simple Gaussian function then the peak area A_G for a given dead time t_{de} can be predicted on the basis of the integral theorem[56] of the Fourier transformation from the decay of the FID.

$$A_G = s_{G,0}\exp[-\lambda_G{}^2 t_{de}{}^2] \quad (4)$$

In order to derive the visibility function $f(x)$ in terms of line-broadening $\lambda_G(x)$, eqn (4) is plugged into the definition of the visibility function.

$$\begin{aligned} f_G(x) \underline{\text{def}} \frac{A_G(x)}{A_G(0)} &= \frac{s_{G,0}\exp\left[-\lambda_G{}^2(x)t_{de}{}^2\right]}{s_{G,0}\exp[-\lambda_G{}^2(0)t_{de}{}^2]} \\ &= \exp\left\{-t_{de}{}^2\left[\lambda_G{}^2(x)-\lambda_G{}^2(0)\right]\right\} \end{aligned} \quad (5)$$

The amplitude factor $s_{G,0}$ of the doped and the pure host material should the equal, while the line width parameter $\lambda_G(x)$ depends on doping concentration. The visibility function can also be expressed in terms of the blind sphere radii r_0, the number density parameter a and doping level x (eqn (1)). Therefore, the link between parameter λ_G and doping level x can be established as follows.

$$\lambda_G{}^2(x) - \lambda_G{}^2(0) = \frac{a r_0{}^3}{t_{de}{}^2}x \quad (6)$$

Assuming a negligible frequency difference between signals, the second moment[48,56] $M_2 = \int\omega^2 I(\omega)\mathrm{d}\omega$ of the Gaussian type function is $2\lambda_G{}^2$ and the second moment becomes $M_2(x) = 2\lambda_G{}^2(x)$. Eqn (6) can be rewritten in terms of the second moment.

$$M_2(x) = M_2(0) + \frac{2a r_0{}^3}{t_{de}{}^2}x \quad (7)$$

A linear regression of the second moment $M_2(x)$ yields the slope $k_G = \frac{2a r_0{}^3}{t_{de}{}^2}$. From the latter the radius of the blind sphere r_0 can be estimated *via* a simple analytical equation.

$$r_0 = \sqrt[3]{\frac{k_G t_{de}{}^2}{2a}} \quad (8)$$

This way the blind-sphere r_0 of Sm^{3+} doped $La_{1-x}Sm_xPO_4$ was estimated to be 0.45 Å. The La to P and Sm to P distances in the monazite[49] structure of $LaPO_4$ and $SmPO_4$ are 3.2 Å and 3.1 Å, respectively, which means that all ^{31}P nuclei are outside of the blind spheres of Sm^{3+} and thus visible. This is consistent with the observation the signal visibility function $f(x)$ remains close to 100% (Fig. 4). In addition, ^{19}F and ^{1}H NMR signals for SmF_3[60] and SmH_3[61,62] both have been reported to be visible, which supports the found small blind sphere size of Sm^{3+}. Given the estimated blind sphere radius is even smaller than the Shannon radius[63] for Sm^{3+} (around 1 Å) it appears that Sm-compounds in general are good candidates for NMR studies, because no signal loss is expected. The second moment analysis as presented above can provide information on the size of the blind sphere, especially for paramagnetic dopants which have small blind spheres.

For Gd^{3+}, the line broadening is mainly based on the homogeneous broadening mechanism which is relaxation dominated and follows a Lorentzian lineshape. Thus the FID can be described with a monoexponentially decaying function. The line width parameter $\lambda_L(x)$ then has a slightly different relation to the blind sphere r_0, doping concentration x and deadtime delay t_{de} (see ESI†).

$$\lambda_L(x) - \lambda_L(0) = \frac{2a r_0{}^3}{t_{de}}x \quad (9)$$

The $\lambda_L(x)$ is related to the full width half-maximum in Hz as $\lambda_L = 2\pi\Delta\nu_L^{FWHM}$.

The relation between the size of blind sphere r_0 and the experimental results $\lambda_L(0)$ (the line width of non-doped diamagnetic analog) and slope k_L value (from the linear fit of $\lambda_L(x)$ against x) can be derived in a similar fashion as in the Gaussian case.

$$r_0 = \sqrt[3]{\frac{k_L t_{de}}{2a}} \quad (10)$$

This way the blind sphere r_0 for the Gd^{3+} doped sample becomes 6.7 Å, which is much smaller than the estimated 13.5 Å from signal visibility method. This discrepancy can be explained by the inadequacy of simple functions to describe the FID. In case the spectral lineshape function becomes more complicated it is non-trivial to extract line-width parameters from the spectra and in those cases the visibility function $f(x)$ provides an easier way to determine blind-sphere radii. As shown above line-shape analysis requires knowledge about the decay character of the FID in order to determine the blind sphere radius. The reported[17,18] linear relation of doping concentration x and linewidth is only expected in case of Lorentzian type spectral lineshapes. While the derivation of blind-spheres *via* a line-shape analysis suffers from a number of approximations including the assumption of a sharp transition of the visible to invisible nuclei, we believe that the scaling behaviour of the doping concentration x with respect to second moment and line-width, is the most important insight that is being conveyed by the above analysis.

Blind sphere radius dependence on the gyromagnetic ratio

In order to investigate the size dependence of the blind sphere on the gyromagnetic ratio γ, data obtained from the same paramagnetic ion but different NMR nuclei are compared (Table 2). In the following we assume that Eu^{2+} and Gd^{3+} are isoelectronic paramagnetic ions, and thus have equal blind sphere radii. The concept of the blind-sphere is based on the idea that the signals of all atoms inside the sphere vanish in the dead-time delay, *i.e.* nuclei which are situated on the blind sphere have a critical relaxation rate, a critical amount of line-broadening or paramagnetic shift. Critical relaxation rates R_{1M} and R_{2M} driven by a dipolar coupling mechanism with unpaired electrons or Curie nuclear spin relaxation are then proportional to $\gamma^2/r_0{}^6$,[39] while critical broadening through the pseudo-contact shift (PCS) relates to $\gamma/r_0{}^3$.[39] Given that other influences, like the spectral density, are negligible, it can be concluded that the prefactors which relate to the critical broadening or

Table 2 The blind sphere radii r_0 values for different NMR nuclei obtained with the visibility method; γ is the nuclei gyromagnetic ratio; $r_0(^{31}P)$ is the blind-sphere radius of a virtual ^{31}P nucleus converted from experimental r_0 *via* the eqn (11)

Host	NMR nucleus	$\gamma/10^7$ rad T^{-1} s^{-1}	$a/Å^{-3}$	Dopant	r_0/Å	$r_0(^{31}P)$/Å
SrH_2	^1H	26.75	0.092	Eu^{2+}	17[21]	12.6
$SrGa_2S_4$	^{71}Ga	8.18	0.025	Eu^{2+}	13	14.3
$LaPO_4$	^{31}P	10.84	0.055	Gd^{3+}	13.5	—
$Zn_3(PO_4)_2{\cdot}4H_2O$	^1H	26.75	0.051	Mn^{2+}	10	7.4
$Zn_3(PO_4)_2{\cdot}4H_2O$	^{31}P	10.84	0.051	Mn^{2+}	7	—

relaxation rate would feature the same relation of gyromagnetic ratio γ to blind sphere radius r_0. In this case the blind sphere radii for different nuclei X and Y in the same compound should feature a cubic root dependence to the gyromagnetic ratio.

$$r_{0,X}/r_{0,Y} = \sqrt[3]{\gamma_X/\gamma_Y} \quad (11)$$

To test this hypothesis we compare blind-sphere radii from different nuclei in the same and in different compounds. The visibility method yielded a blind sphere radius from ^{71}Ga NMR for Eu^{2+} in $Sr_{1-x}Eu_xGa_2S_4$ (Fig. 7). This may be compared with a blind sphere for Eu^{2+} in $Sr_{1-x}Eu_xH_2$ from ^1H NMR[21] and with one for Gd^{3+} in $La_{1-x}Gd_xPO_4$ from ^{31}P NMR (Fig. 2). The values converted to the blind sphere *via* eqn (11) of a virtual ^{31}P nucleus are the same (Table 2) within approximated error limits. Given the low number of values in the comparison this is a weak indication that the blind sphere radii of lanthanide dopants may be abstracted from the host structure.

In a second example the sphere radius of Mn^{2+} is detected by ^1H and ^{31}P NMR in hopeite $(Zn_{1-x}Mn_x)_3(PO_4)_2{\cdot}4H_2O$ (Fig. 8). Again the virtual radius of ^{31}P converted from the radius applying to the ^1H nucleus agrees to the observed value within error limits (Table 2). Deviations from this fairly good agreement are expected especially in case of a Fermi-contact contribution[64,65] which however does not seem to be relevant here. Another explanation in case of a relaxation dominated blind sphere may be the change of the electronic relaxation mechanism at high doping concentrations which in principle could even lead to an increase visibility in the high concentration regime. In some cases of transition metal doping even at very high dopant concentration[64,65] the signal does not vanish.

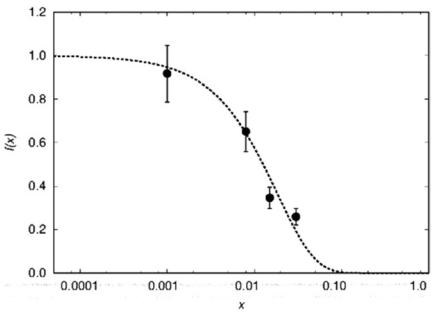

Fig. 7 Normalized NMR visibility function $f(x)$ on a logarithmic scale for x for $Sr_{1-x}Eu_xGa_2S_4$ (circles). The dashed line corresponds to the fitted function $f(x) = \exp(-ar_0^3x)$ with a = 0.025/Å^3 and r_0 = 13 Å.

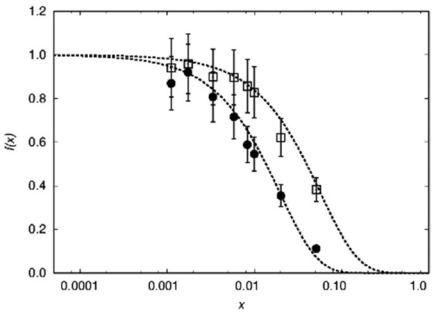

Fig. 8 Normalized NMR visibility function $f(x)$ on a logarithmic scale for x for $(Zn_{1-x}Mn_x)_3(PO_4)_2{\cdot}4H_2O$. $f(x)$ data obtained from ^1H NMR are plotted as circles while those from ^{31}P NMR as squares. The dashed lines feature the fitted functions $f(x) = \exp(-ar_0^3x)$ with a = 0.051/Å^3, r_0 = 10 Å and 7 Å for ^1H and ^{31}P, respectively.

In the presented cases of lanthanide(III) doped monazite the only system where we have an indication of a relaxation dominated blind sphere radius is Gd(III). At 100% doping, *i.e.* pure $GdPO_4$ no intensity increase can be observed, in line with the presented interpretation.

Blind sphere radius dependence on the effective magnetic moment

In order to test the hypothesis that blind sphere radius depends on the effective magnetic moment, data obtained from the same host $LaPO_4$ and the same NMR nucleus (^{31}P) but different paramagnetic dopants are compared. Relaxation and hyperfine shift are two possible origins of blind spheres, and are discussed resonances in $La_{1-x}Ln_xPO_4$ are inhomogeneously broadened for all Ln^{3+} dopants except Gd^{3+}, which indicates that relaxation is dominant in the case of doping by Gd^{3+} but not as important in case of other paramagnetic Ln^{3+} as is explained in detail in the following paragraph.

Relaxation

Dipolar, Curie-spin and Fermi-contact relaxation are in principle three possible relaxation contributions in paramagnetic systems which lead to homogeneous line broadening. For solid crystalline $La_{1-x}Ln_xPO_4$, chemical exchange and stochastic reorientation are negligible, only vibrational motions exert efficient influence on the electronic relaxation. Based on the Solomon–Bloembergen–Morgan relaxation model,[66,67] the nuclear transverse relaxation time T_2 can be described as eqn (12) for lanthanide ions induced paramagnetic relaxation enhancement (PRE). Parameter A^{FC} is the Fermi-contact coupling and $b_{JI} = \frac{\mu_0\mu_B g_J \hbar \gamma_I}{4\pi R^3}$ is the spin-dipolar coupling parameter.[67] T_{1e} and T_{2e} are the longitudinal and transverse electronic relaxation times, respectively, which are used to approximate the corresponding electronic correlation times.[67] ω_I and ω_S are the nuclear and electronic Larmor frequencies, respectively. J is the main total angular momentum quantum number. R is the distance between NMR nuclei and the unpaired electrons which belong to the paramagnetic ion and are assumed to be localized on the lanthanide ion (point-dipole approximation).

The γ_I is the nuclear gyromagnetic ratio and g_J is the isotropic Born–Landé g-factor.

$$\frac{1}{T_2} = \frac{1}{3}J(J+1)\left(\frac{A^{FC}}{\hbar}\right)^2\left[T_{1e} + \frac{T_{2e}}{1+(\omega_S-\omega_I)^2 T_{2e}^2}\right] + \frac{1}{15}J(J+1)\left(\frac{b_{JI}}{\hbar}\right)^2\left[4T_{1e} + \frac{6T_{2e}}{1+\omega_S^2 T_{2e}^2} + \frac{3T_{1e}}{1+\omega_I^2 T_{1e}^2} + \frac{6T_{2e}}{1+(\omega_S+\omega_I)^2 T_{2e}^2} + \frac{T_{2e}}{1+(\omega_S-\omega_I)^2 T_{2e}^2}\right] \quad (12)$$

The first term in this equation is caused by Fermi-contact coupling and lacks a simple relation to the blind-sphere radius. The second term, called pseudo-contact term, is caused by a direct dipole–dipole interaction and has a distance dependence of R^{-6}. At the critical relaxation rate (neglecting the Fermi contact contribution) the second term is proportional to $b_{JI}^2 J(J+1)$ or expressed with the effective magnetic moment $\mu_{eff} = g_J\mu_B\sqrt{J(J+1)}$ (Landé formula) proportional to $\mu_{eff}^2 R^{-6}$. The electronic relaxation times in solids are driven by vibrational motions and differ by the lanthanide ion. Published ranges[39,67] of the electronic relaxation times show only minor differences for lanthanides Ln^{3+} (Ln = Sm, Nd, Yb, Tm, Er and Ho) with the exception of Gd^{3+} (see Table 8.6 in ref. 67) for which electronic relaxation rates are several orders of magnitude lower than for the other paramagnetic lanthanide ions, which causes efficient nuclear transversal relaxation and is consistent with the magnitude of the linewidth (few hundreds to kHz) observed from the EXSY (Fig. 6) and single pulse measurements. Note that the EXSY experiment with a very short mixing time behaves like a stimulated echo and provides information about transversal relaxation over the complete linewidth. For the other Ln^{3+} ions, the observed line broadening (Fig. 6 and ESI,† Fig. S2) is of the order of ten to a hundred Hz. This is much larger than the expected relaxation-induced line broadening which indicates relaxation not to be the predominant source of broadening. This interpretation is in agreement with the observation that the line broadening for Gd^{3+} is homogeneous while the other Ln^{3+} dopants generate inhomogeneous line broadening and explains the exceptional role of Gd^{3+} in the Fig. 9 and 10.

Paramagnetic shift

Besides relaxation, another possible origin for blind sphere is the paramagnetic shift δ_{param}. The inhomogeneous line-broadening observed on the ^{31}P resonances indicates that the paramagnetic shift is the relevant origin for the blind spheres of $LaPO_4$ doped with Ln^{3+} (Ln = Nd, Sm, Dy, Er, Ho, Tm, Yb), but not for $LaPO_4$ doped with Gd^{3+}. Different mechanisms may cause a paramagnetic isotropic or anisotropic shift, which have been subject to a recent review.[67] In order to compare the relative size of paramagnetic shift in a lanthanide series Bleaney,[68] Golding and Halton[69] have developed an approach in which they separate the electronic term C from a coupling term.

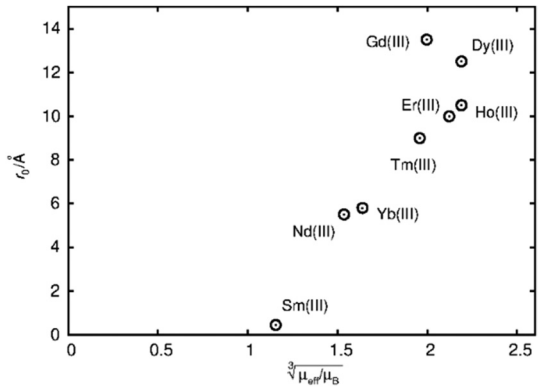

Fig. 9 Blind sphere radii for Ln(III) dopants of $La_{1-x}Ln_xPO_4$ series, plotted against $\sqrt[3]{\mu_{eff}/\mu_B}$. The μ_{eff} and μ_B refer to effective magnetic moment[53] and Bohr magneton, respectively.

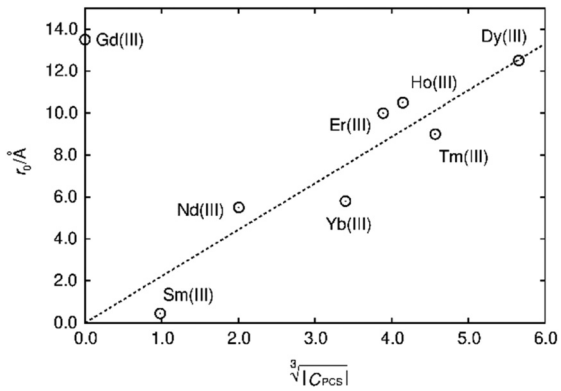

Fig. 10 Blind sphere radii for Ln(III) dopants of $La_{1-x}Ln_xPO_4$ series, plotted against $\sqrt[3]{|C_{PCS}|}$. $|C_{PCS}|$ refers to the magnitude of electronic contribution from pseudo-contact shielding.[67,68] The dashed line features the fitting function $r_0/\text{Å} = 2.22 \cdot \sqrt[3]{|C_{PCS}|}$ with the coefficient of determination $R^2 = 0.89$.

The size of the electronic term can be described by a real number and was tabulated by Pell *et al.*[67] for the contact shift C_{con}, the pseudo-contact shift $C_{PCS} = g^2J(J+1)(2J-1)(2J+3)\langle J||\alpha||J\rangle$[67] and the shielding anisotropy C_{SA} (Table 3). Given that a critical broadening or shift exists (see above) which defines the blind-sphere radius r_0, it should be possible to obtain a linear relation between $\sqrt[3]{|C_{PCS}|}$ and the blind sphere radius r_0. In fact a good correlation is observed (Fig. 10), with the expected exception of Gd^{3+} (see above). For completeness we have also plotted the blind-sphere radius *vs.* $\sqrt[3]{|C_{SA}|}$ (ESI,† Fig. S3) and $\sqrt[3]{|C_{con}|}$ (Fig. S4, ESI†). The observed excellent empirical correlation in case of the contact interaction lacks a good explanation, though. It should not be overinterpreted as it is caused by the drastic change of a single measurement, *i.e.* on $La_{1-x}Gd_xPO_4$ for which relaxation is expected to have a big influence.

To sum up, for Ln^{3+} both relaxation (in case of Gd^{3+}) and the paramagnetic shift (in case of the other presented Ln^{3+}) give an explanation for the origin of the blind sphere. The pseudo-contact term provides a simple explanation for the change of

Table 3 Radii of blind spheres r_0 obtained from ^{31}P MAS NMR of $La_{1-x}Ln_xPO_4$ sample series, and corresponding Ln^{3+} hyperfine contributions.[67] $|C_{SA}|$, $|C_{con}|$ and $|C_{PCS}|$ refer to the electronic contribution to the paramagnetic shift from shielding anisotropy, contact and pseudo-contact term, respectively

Dopant ion	r_0^A/Å	$\lvert C_{SA}\rvert$	$\lvert C_{con}\rvert$	$\lvert C_{PCS}\rvert$
Nd^{3+}	5.5	13.1	4.5	8.08
Sm^{3+}	0.45	0.7	0.063	0.94
Gd^{3+}	13.5	63	31.5	0
Dy^{3+}	12.5	113.3	28.5	181
Ho^{3+}	10.5	112.5	22.6	71.3
Er^{3+}	10.0	91.8	15.4	58.8
Tm^{3+}	9.0	57.2	8.2	95.3
Yb^{3+}	5.8	20.6	2.6	39.2

the blind-sphere radius in a lanthanide series and predicts a $r_0 \propto \sqrt[3]{|\mu_{eff}|}$ dependence for relaxation and a $r_0 \propto \sqrt[3]{|C_{PCS}|}$ dependence for the paramagnetic shift, of which the latter is confirmed by the experiment.

Conclusions

In this work, sizes of blind spheres r_0 have been determined from NMR spectra by two methods: signal visibility decay function and lineshape analysis. A formula for the blind sphere radius could be derived, that relates the radii of blind sphere to the lineshape for a given dead time of the spectrometer, which allows to estimate blind-sphere radii even when the visibility remains close to 100% over the complete doping range.

The dependence of blind sphere radii on the effective magnetic moment of the dopant ions and on the nucleus give insight into processes leading to a blind-sphere and provide estimates for blind sphere radii upon switching the dopant in a lanthanide series or the nucleus. Blind-sphere radii up to 13 Å suggest that a significant amount of material may remain virtually invisible in NMR, while certain paramagnetic ions, like Sm^{3+}, allow the detection of NMR signal even from atoms two bonds away from paramagnetic centre. These results are relevant for evaluating the paramagnetic doping homogeneity of inorganic phosphors and their optical performance and to estimate which nuclei around a paramagnetic centre can directly be observed, for example in dynamic nuclear polarization (DNP) NMR or by direct detection.

Conflicts of interest

There are no conflicts to declare.

References

1 I. Bertini, P. Turano and A. J. Vila, *Chem. Rev.*, 1993, **93**, 2833–2932.
2 I. Bertini, C. O. Fernández, B. G. Karlsson, J. Leckner, C. Luchinat, B. G. Malmström, A. M. Nersissian, R. Pierattelli, E. Shipp, J. S. Valentine and A. J. Vila, *J. Am. Chem. Soc.*, 2000, **122**, 3701–3707.
3 C. Öster, S. Kosol, C. Hartlmüller, J. M. Lamley, D. Iuga, A. Oss, M.-L. Org, K. Vanatalu, A. Samoson, T. Madl and J. R. Lewandowski, *J. Am. Chem. Soc.*, 2017, **139**, 12165–12174.
4 E. Ravera, G. Parigi and C. Luchinat, *J. Magn. Reson.*, 2017, **282**, 154–169.
5 L. Cerofolini, T. Staderini, S. Giuntini, E. Ravera, M. Fragai, G. Parigi, R. Pierattelli and C. Luchinat, *JBIC, J. Biol. Inorg. Chem.*, 2018, **23**, 71–80.
6 J. Kim, D. S. Middlemiss, N. A. Chernova, B. Y. X. Zhu, C. Masquelier and C. P. Grey, *J. Am. Chem. Soc.*, 2010, **132**, 16825–16840.
7 L. Zhou, M. Leskes, A. J. Ilott, N. M. Trease and C. P. Grey, *J. Magn. Reson.*, 2013, **234**, 44–57.
8 X. Li, M. Tang, X. Feng, I. Hung, A. Rose, P.-H. Chien, Z. Gan and Y.-Y. Hu, *Chem. Mater.*, 2017, **29**, 8282–8291.
9 C. A. Lepre, J. M. Moore and J. W. Peng, *Chem. Rev.*, 2004, **104**, 3641–3676.
10 Q. Z. Ni, F. Yang, T. V. Can, I. V. Sergeyev, S. M. D'Addio, S. K. Jawla, Y. Li, M. P. Lipert, W. Xu, R. T. Williamson, A. Leone, R. G. Griffin and Y. Su, *J. Phys. Chem. B*, 2017, **121**, 8132–8141.
11 R. R. Amirov, E. A. Burilova, Y. I. Zhuravleva, A. V. Zakharov and A. B. Ziyatdinova, *Polym. Sci., Ser. C*, 2017, **59**, 133–140.
12 N. J. Brownbill, R. S. Sprick, B. Bonillo, S. Pawsey, F. Aussenac, A. J. Fielding, A. I. Cooper and F. Blanc, *Macromolecules*, 2018, **51**, 3088–3096.
13 C. S. Zuo, K. R. Metz, Y. Sun and A. D. Sherry, *J. Magn. Reson.*, 1998, **133**, 53–60.
14 A. E. Thorarinsdottir, A. I. Gaudette and T. David Harris, *Chem. Sci.*, 2017, **8**, 2448–2456.
15 M. Ilibi, T. B. de Queiroz, J. Ren, L. D. Cola, A. S. S. de Camargo and H. Eckert, *Dalton Trans.*, 2014, **43**, 8318–8330.
16 M. de Oliveira, T. Uesbeck, T. S. Gonçalves, C. J. Magon, P. S. Pizani, A. S. S. de Camargo and H. Eckert, *J. Phys. Chem. C*, 2015, **119**, 24574–24587.
17 T. Harazono, E. Yokota, H. Uchida and T. Watanabe, *Bull. Chem. Soc. Jpn.*, 1998, **71**, 2797–2805.
18 T. Harazono, E. Yokota, H. Uchida and T. Watanabe, *Bull. Chem. Soc. Jpn.*, 1998, **71**, 825–829.
19 T. Harazono, R. Adachi, N. Kijima and T. Watanabe, *Bull. Chem. Soc. Jpn.*, 1999, **72**, 2655–2664.
20 S. Maron, G. Dantelle, T. Gacoin and F. Devreux, *Phys. Chem. Chem. Phys.*, 2014, **16**, 18788–18798.
21 W. Li, V. R. Celinski, J. Weber, N. Kunkel, H. Kohlmann and J. Schmedt auf der Günne, *Phys. Chem. Chem. Phys.*, 2016, **18**, 9752–9757.
22 S. Maron, N. Ollier, T. Gacoin and G. Dantelle, *Phys. Chem. Chem. Phys.*, 2017, **19**, 12175–12184.
23 N. C. George, J. Brgoch, A. J. Pell, C. Cozzan, A. Jaffe, G. Dantelle, A. Llobet, G. Pintacuda, R. Seshadri and B. F. Chmelka, *Chem. Mater.*, 2017, **29**, 3538–3546.
24 L. Russo, M. Maestre-Martinez, S. Wolff, S. Becker and C. Griesinger, *J. Am. Chem. Soc.*, 2013, **135**, 17111–17120.
25 R. J. McCarty and J. F. Stebbins, *Solid State Nucl. Magn. Reson.*, 2016, **79**, 11–22.
26 C. P. Grey, C. M. Dobson, A. K. Cheetham and R. J. B. Jakeman, *J. Am. Chem. Soc.*, 1989, **111**, 505–511.

27 T. Wittmann, A. Mondal, C. B. L. Tschense, J. J. Wittmann, O. Klimm, R. Siegel, B. Corzilius, B. Weber, M. Kaupp and J. Senker, *J. Am. Chem. Soc.*, 2018, **140**, 2135–2144.
28 A. Mondal, M. W. Gaultois, A. J. Pell, M. Iannuzzi, C. P. Grey, J. Hutter and M. Kaupp, *J. Chem. Theory Comput.*, 2018, **14**, 377–394.
29 A. R. Brough, C. P. Grey and C. M. Dobson, *J. Am. Chem. Soc.*, 1993, **115**, 7318–7327.
30 J. H. Van Vleck, *Phys. Rev.*, 1948, **74**, 1168–1183.
31 P. W. Anderson and P. R. Weiss, *Rev. Mod. Phys.*, 1953, **25**, 269–276.
32 G. W. Parker and F. Lado, *Phys. Rev. B: Solid State*, 1973, **8**, 3081–3092.
33 C. Zhang, T. Uchikoshi, L. Liu, B. Dierre, Y. Sakka and N. Hirosaki, *Appl. Phys. Lett.*, 2014, **104**, 021914.
34 L. I. D. J. Martin, D. Poelman, P. F. Smet and J. J. Joos, *ECS J. Solid State Sci. Technol.*, 2018, **7**, R3052–R3056.
35 V. Bachmann, C. Ronda, O. Oeckler, W. Schnick and A. Meijerink, *Chem. Mater.*, 2009, **21**, 316–325.
36 J. J. Joos, K. W. Meert, A. B. Parmentier, D. Poelman and P. F. Smet, *Opt. Mater.*, 2012, **34**, 1902–1907.
37 V. Bachmann, C. Ronda and A. Meijerink, *Chem. Mater.*, 2009, **21**, 2077–2084.
38 I. Bertini, C. Luchinat, G. Parigi and R. Pierattelli, *ChemBioChem*, 2005, **6**, 1536–1549.
39 I. Bertini, C. Luchinat, G. Parigi and E. Ravera, *NMR of Paramagnetic Molecules: Applications to Metallobiomolecules and Models*, Elsevier, 2016.
40 I. J. Lowe and D. Tse, *Phys. Rev.*, 1968, **166**, 279–291.
41 B. Giovannini, P. Pincus, G. Gladstone and A. J. Heeger, *J. Phys., Colloq.*, 1971, **32**, C1-163.
42 M. Punkkinen, *Phys. Kondens. Mater.*, 1971, **13**, 79–88.
43 B. Corzilius, L. B. Andreas, A. A. Smith, Q. Z. Ni and R. G. Griffin, *J. Magn. Reson.*, 2014, **240**, 113–123.
44 R. Rogawski, I. V. Sergeyev, Y. Zhang, T. H. Tran, Y. Li, L. Tong and A. E. McDermott, *J. Phys. Chem. B*, 2017, **121**, 10770–10781.
45 T. Wolf, S. Kumar, H. Singh, T. Chakrabarty, F. Aussenac, A. I. Frenkel, D. T. Major and M. Leskes, *J. Am. Chem. Soc.*, 2019, **141**, 451–462.
46 A. Bertarello and G. Pintacuda, *Paramagnetism in Experimental Biomolecular NMR*, 2018, pp. 163–188.
47 S. Lange, A. H. Linden, Ü. Akbey, W. Trent Franks, N. M. Loening, B. J. van Rossum and H. Oschkinat, *J. Magn. Reson.*, 2012, **216**, 209–212.
48 D. Jardón-Álvarez and J. Schmedt auf der Günne, *Solid State Nucl. Magn. Reson.*, 2018, **94**, 26–30.
49 Y. Ni, J. M. Hughes and A. N. Mariano, *Am. Mineral.*, 1995, **80**, 21–26.
50 A. C. Palke, J. F. Stebbins and L. A. Boatner, *Inorg. Chem.*, 2013, **52**, 12605–12615.
51 J. F. Stebbins, R. J. McCarty and A. C. Palke, *Acta Crystallogr., Sect. C: Struct. Chem.*, 2017, **73**, 128–136.
52 L. Vegard, *Z. Phys.*, 1921, **5**, 17–26.
53 C. H. Evans, *Biochemistry of the Lanthanides*, Springer Science & Business Media, 2013.
54 G. E. Pake and E. M. Purcell, *Phys. Rev.*, 1948, **74**, 1184–1188.
55 M. M. Maricq and J. S. Waugh, *J. Chem. Phys.*, 1979, **70**, 3300–3316.
56 K. Schmidt-Rohr and H. W. Spiess, *Multidimensional Solid-State NMR and Polymers*, Elsevier, 2012.
57 N. Bloembergen, E. M. Purcell and R. V. Pound, *Phys. Rev.*, 1948, **73**, 679–712.
58 G. A. Morris and R. Freeman, *J. Magn. Reson.*, 1969, **1978**(29), 433–462.
59 P. L. Kuhns and M. S. Conradi, *J. Chem. Phys.*, 1982, **77**, 1771–1778.
60 A. Y. H. Lo, V. Sudarsan, S. Sivakumar, F. van Veggel and R. W. Schurko, *J. Am. Chem. Soc.*, 2007, **129**, 4687–4700.
61 O. J. Żogał, M. Drulis and S. Idziak, *Z. Phys. Chem.*, 1989, **163**, 303–308.
62 O. J. Żogał, S. Idziak, M. Drulis and K. Niedźwiedź, *Phys. Status Solidi B*, 1991, **167**, K55–K58.
63 R. D. Shannon, *Acta Crystallogr., Sect. A: Cryst. Phys., Diffr., Theor. Gen. Crystallogr.*, 1976, **32**, 751–767.
64 F. C. Strobridge, D. S. Middlemiss, A. J. Pell, M. Leskes, R. J. Clément, F. Pourpoint, Z. Lu, J. V. Hanna, G. Pintacuda, L. Emsley, A. Samoson and C. P. Grey, *J. Mater. Chem. A*, 2014, **2**, 11948–11957.
65 I. D. Seymour, D. S. Middlemiss, D. M. Halat, N. M. Trease, A. J. Pell and C. P. Grey, *J. Am. Chem. Soc.*, 2016, **138**, 9405–9408.
66 N. Bloembergen and L. O. Morgan, *J. Chem. Phys.*, 1961, **34**, 842–850.
67 A. J. Pell, G. Pintacuda and C. P. Grey, *Prog. Nucl. Magn. Reson. Spectrosc.*, 2019, **111**, 1–271.
68 B. Bleaney, *J. Magn. Reson.*, 1972, **8**, 91–100.
69 R. M. Golding and M. P. Halton, *Aust. J. Chem.*, 1972, **25**, 2577–2581.

